ADVANCED ELECTRONIC MATERIALS
www.advelectronicmat.de

Constructing Metal Arch Nanobridges Utilizing a Photothermal-Induced Nanobonding Technique

*Pintu Ghosh, Jinsheng Lu, Hao Luo, Wei Wang, Ziquan Xu, Min Qiu, and Qiang Li**

Construction of multilayered arch nanobridges and nanocantilever structures consisting of silver nanowires using a photothermal-induced nanobonding technique is demonstrated. The fabricated nanobridges are of different height (300 nm to 20 µm) and span (25–70 µm). Their current–voltage characteristic curves indicate superior electrical connection between the metal nanowires and the abutments (gold thin film). Moreover, super mechanical strength of these arch nanobridges and nanocantilevers is demonstrated by putting gold nanoplates (a few tens of nm thick, a few tens of µm in diameter, and a maximum weight of 3 pN—about 20 times heavier than the silver nanowire of same length) on top of these nanostructures. The multilayered arch nanobridges demonstrate their potential applicability as short-circuit-free multipronged electronic connections in nanoelectronic devices. Furthermore, by recording the change in vibration frequency due to proximity of foreign contamination, these nanobridges and the nanocantilevers can be utilized to identify them; that is, these nanostructures can be used as biological sensors to detect viruses, bacteria, and other pathogens.

The construction of arch bridges, which can today be found all across the world, has a long interesting history, and possibly the oldest existing arch bridge, Mycenaean Arkadiko bridge in Greece from about 1300 BC,[1] is still used by the local populace. The curved design of an arch bridge allows it not to push load forces straight down, but instead they are transmitted along the curve of the arch to the supports (called abutments) at either end. Its weight pushes the abutments down and outward, making the entire structure extensively rigid and strong. This type of arch bridge at nanoscale (we call it arch nanobridge) is also of paramount importance as they can potentially be applied in manufacturing and maintenance of nanoelectronic, nanophotonic, and nanomechanical devices, such as nanowire networks and interconnects,[2,3] quantum interference device,[4] photodetector,[5] and phototransistor.[6] In particular, the arch shape enables it to avoid short-circuit and any other physical nano-obstacles in nanodevices.

In last few decades, quite a few researchers have fabricated nanobridges successfully following different methods: (1) molecular beam epitaxy (MBE): arch-shaped nanobridge with height (h) and span (S) ≈ 2 µm;[3] (2) electron beam lithography (EBL): straight nanobridge with S ≈ 2 µm;[4,7] (3) chemical-mechanical polishing (CMP): straight nanobridge with h ≈ 20 nm and S ≈ 1 µm;[8] (4) metal-induced growth: straight nanobridge with S ≈ 1 µm;[2] (5) thermal oxidation: straight nanobridge with S ≈ 200 nm;[5] (6) vapor-liquid-solid growth: straight nanobridge with S ≈ 4–11 µm.[6] EBL, MBE, and CMP provide high accuracy in spatial position selection of the nanobridges, but they involve highly expensive and complex experimental setup. The other methods, which are mentioned above, are relatively less expensive but can hardly be applied for precisely positioning the nanobridges and also have limited flexibility in terms of deciding the height and span, which limits their applicability. Moreover, most of these methods are utilized for fabrication of straight nanobridges and not suitable for fabrication of arch-shaped nanobridges. Although Lewis et al.,[3] have reported fabrication of arch nanobridges utilizing an innovative method of strain engineering, it necessitates complex growth of two lattice mismatched and highly asymmetric core–shell structures using MBE. Therefore, it is of great interest to develop a relatively simpler method to fabricate arch-shaped nanobridges.

In this article, we demonstrate fabrication of multilayered arch nanobridges and nanocantilevers by utilizing photothermal-induced nanobonding technique. To realize the fabrication of an arch nanobridge with a relatively simple method, we improvised a technique where we raise the central part of a metal nanowire (NW) in an arch form using a nanofiber and fix the two ends on two different electrodes by continuous wave (CW) laser based photothermal-induced nanobonding technique which provides many advantages over other techniques (thermal,[9] photothermal,[10–18] capillarity-driven,[19,20] chemical,[21–23] electrochemical,[24] stretch-induced,[25–28] mechanical pressing,[29] nanosoldering,[30–32] and Joule heating.[33,34]) in terms of relatively simple experimental setup, spatial position selection, noncontact handling, and cost effectiveness.[35–37]

Dr. P. Ghosh, J. Lu, H. Luo, Dr. W. Wang, Z. Xu, Prof. M. Qiu, Prof. Q. Li
State Key Laboratory of Modern Optical Instrumentation
College of Optical Science and Engineering
Zhejiang University
Hangzhou 310027, P. R. China
E-mail: qiangli@zju.edu.cn
Prof. M. Qiu
Institute of Advanced Technology
Westlake Institute for Advanced Study
Westlake University
Hangzhou 310024, P. R. China
The ORCID identification number(s) for the author(s) of this article can be found under https://doi.org/10.1002/aelm.201800807.

DOI: 10.1002/aelm.201800807

Thereafter, current–voltage characteristic curves of the arch nanobridges are also recorded toward realizing their potential application in fabrication and maintenance of nanoelectronic devices. We also demonstrate their super mechanical strength by putting weight on top of the arch nanobridges, and also use them as stand to hold micro-objects. For example, gold nanoplates (GNPs, a few tens of nm thick, a few tens of μm in diameter, and a maximum weight of 3 pN—about 20 times heavier than the silver nanowire of the same length) which can be used as microreflectors for visible light, are placed on top of the arch nanobridges and nanocantilevers. The adhesive force between the GNP and the NW is strong enough to keep the GNPs suspended in the air in a stable configuration. The multilayered arch nanobridges demonstrate their potential applicability as short-circuit-free multipronged electronic connections in nanoelectronic devices. Furthermore, by recording the change in vibration frequency due to proximity of contamination, these nanobridges and the nanocantilevers can be utilized as biological sensors.

Toward realizing fabrication of any complex nanostructures, Ag NW comes to mind immediately due to the recent advances in synthesis of long (a few tens of μm) NWs, which find application in diverse fields of nanoscience and nanotechnology,[38–40] including nanoelectronics,[17,18,37] nanophotonics,[41,42] and nanomechanical systems.[43–45] Silver is specifically an attractive material for fabricating arch nanobridges because it is an extremely soft, ductile, and malleable transition metal, which also exhibits the highest electrical and thermal conductivities among all metals. It should also be mentioned that silver nanowire has comparable hardness and elastic modulus to bulk silver.[46]

The fabrication of an arch nanobridge is realized by raising the central part of an Ag NW in an arch form using a nanofiber and by fixing the two ends on two different metal abutments (gold thin films) by photothermal-induced nanobonding technique. A focused CW laser (λ = 532 nm) shot (duration τ = 4 ms) is used for bonding the ends of an Ag NW on a gold thin film (thickness ≈ 100 nm) deposited on silica substrate. A microscope objective (100×) is used to focus the laser beam (waist ≈ 400 nm), which makes the bonding process energy-efficient and precise. The sample is also mounted on a 3D scanning stage (least step size = 30 nm) to move the desired point of the NW accurately to the focus point. The laser polarization and power are manipulated by using a combination of two polarizers and one half-wave plate. More details about the experimental setup can be found in Figure S1 (Supporting Information).

In photothermal-induced nanobonding technique, optical energy is converted to thermal energy when photons are absorbed due to the excitation of surface plasmon polaritons on the metal NW. This thermal energy increases the temperatures of the Ag NW and the Au thin film, which in turn melt the contacting surfaces when the temperatures of the materials reach close to their melting points. The atoms of the melted NW and the gold thin film get diffused, and upon cooling they solidify and become rigidly bonded together. High-resolution transmission electron microscopy images of the bonding are provided in Figure S2 (Supporting Information). Photothermal-induced bonding of an Ag NW on an Au thin film is obtained by exposing the NW placed on the Au thin film to a focused CW laser shot (**Figure 1**a–c). Both perpendicular and parallel (electric field of the incident laser beam is perpendicular/parallel to the long axis of the NW) polarizations can be used to bond an Ag NW on a gold thin film. Figure 1d–i shows the scanning electron microscopy (SEM) images of the bonded Ag NW on a gold thin film corresponding to different polarizations. The top view of the SEM images shows that the NW becomes thinner at focal point of the laser beam (Figure 1d,g). As shown in the figure, the initial diameter ($D \approx 280$ nm) of the Ag NW near the focal point of the laser beam reduces to 260 and 245 nm for the parallel and perpendicular polarizations of the incident laser beam with power P = 120 and 90 mW, respectively. This reduction of diameter after laser exposure indicates melting of the surface of the Ag NW. Although the laser power is much lower in case of perpendicular polarization, it is noted that the reduction of the NW diameter is more for this polarization, indicating that the melting of the surface of the Ag NW is more sensitive to perpendicular polarization. The tilt- and cross-section-view SEM images show that a hemispherical hollow bump of the gold thin film is formed for both polarizations (Figure 1e,f,h,i). The laser being Gaussian in shape, the absorbed energy, and corresponding temperature of the gold thin film are the highest at the center of the laser beam spot, and they decay drastically outside the laser beam spot. Therefore, the gold thin film expands more at the center of the laser beam spot, whereas the film remains in mechanical contact with the silica substrate outside the spot. This thermal expansion of the gold thin film due to the high local temperature leads to the formation of the bump. The height and diameter of the bump for optimum power corresponding to both polarizations of the incident laser beam are ≈360 nm and 4.5 μm, respectively. This bump is not essential to realize the arch shape of the nanobridge, but it works like a ramp and helps in forming the arch without breaking the NW due to stress arising from sharp bending, specifically when the height of the arch nanobridge is about a few hundreds of nm, as the height of the bump is of the same order. The similar size of the bumps for both polarizations in spite of using much lower power for perpendicular polarization compared to parallel polarization indicates that the bonding process is more energy-efficient for perpendicular polarization. The reduction of diameters of different NWs near the focal point of the laser beam (perpendicular polarization) is plotted with respect to the laser power (Figure 1j). For any particular polarization, we start with a very low power and thereafter keep increasing the power until we obtain optimum bonding of the Ag NW on the gold thin film. If we keep increasing the laser power further, the NW breaks.[47] Optimum bonding is obtained for the power range when it is high enough to melt the surface of the NW and the gold thin film but less than the power which initiates the breaking of the NW. The recorded optimum power range is much lower for perpendicular polarization compared to parallel polarization. Therefore, we preferred perpendicular polarization for bonding of the Ag NW on the gold thin film toward fabricating different arch bridges. It is observed that the optimum power range increases with the diameter of the NW, which can be understood intuitively—for larger diameter, there are more silver atoms which can melt and participate in the bonding process. For example, the optimum power ranges for NWs with

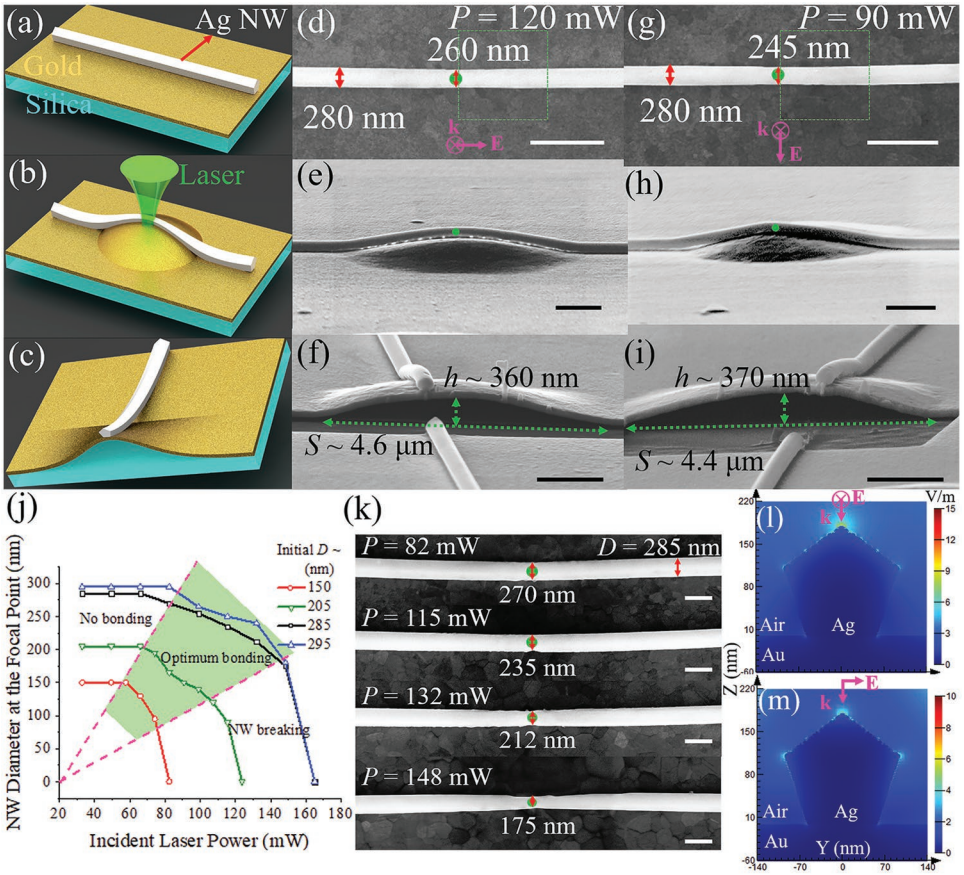

Figure 1. Nanobonding. Schematic diagrams depicting a) the initial state of an Ag NW placed on a gold thin film, b) formation of a hemispherical bump when the Ag NW is subjected to CW laser exposure, and c) the cross-section view of the bump. SEM images showing the bonding of the Ag NW with the gold thin film for d–f) parallel and g–i) perpendicular polarizations of the incident laser beam. The polarizations of the laser beam are represented by pink arrows. SEM images of (d, g) top-, (e, h) tilt-, and (f, i) cross-section views of the bonded NWs. The images of cross-section views are recorded after removing half of the bump including the NW (indicated by the green dashed boxes in (d) and (g)) using focused ion beam. The scale bars are 1 μm. j) NW diameter at the focal point versus incident laser (perpendicular polarization) power plot for different NWs. The shaded region shows the optimum power range. k) Top-view SEM images showing the change in diameter near the focal point for the optimum laser power range corresponding to perpendicular polarization. The scale bars are 400 nm. Simulated dominant component of the electric field distribution for l) parallel and m) perpendicular polarizations, respectively. The tilt angle for tilt- and cross-section views is set at 75°. The green dots indicate the laser incident position.

diameters 150 and 295 nm are 55–75 and 85–150 mW, respectively. Representatively, the top-view SEM images showing the change in diameter of an Ag NW (initial $D \approx 285$ nm) for the optimum power range ($P_{range} \approx 80$–150 mW) corresponding to perpendicular polarization are shown in Figure 1k. The SEM images showing change in diameter for the optimum power range for different NWs are provided in Figure S3 (Supporting Information). This wide optimum power range makes this bonding technique easy to achieve for NWs with a broad range of diameters.

Toward better understanding of this polarization effect on bonding, we simulated the light absorption fraction and electric field distribution for both the polarizations using finite-difference time-domain (FDTD) Lumerical software. The fraction of power from the source that is absorbed within the volume corresponding to parallel and perpendicular polarizations are ≈13 and 48%, respectively (see the Experimental Section for further details). This stronger absorption makes the perpendicular polarization more energy-efficient. Furthermore, we analyze the electric field distribution of the plasmonic modes for both perpendicular and parallel polarizations (Figure 1l,m). The figures show that different plasmonic modes are excited for different polarizations.[48,49] The mode excited for perpendicular polarization is more lossy, which makes this polarization more energy-efficient compared to the parallel polarization.

A single arch bridge consisting of a single Ag NW is fabricated by raising the central part of the NW by a nanofiber in an arch shape and welding the two ends of the NW on two gold electrodes (**Figure 2**a). The fabrication procedure of a single arch bridge can be enlisted in several steps (schematic diagrams are provided in Figure S4, Supporting Information). First, the Ag (synthesized by a self-seeding approach)[50] NW is placed between two adjacent Au electrodes in such a way that the central part of the NW is at around the midpoint of the gap between the electrodes. These microgap Au electrodes are fabricated using a focused ion beam (FIB) on a 100-nm-thick gold film deposited on the silica substrate. The gap between two adjacent electrodes is varied between 10 and 50 μm according to the

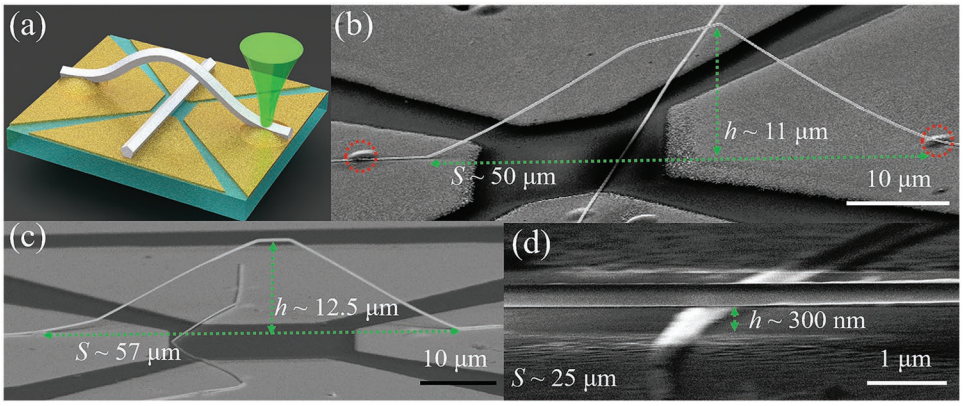

Figure 2. Single arch nanobridge. a) Schematic diagram of a single arch bridge formed by photothermal-induced bonding of silver NW on gold thin film at two ends of the NW. b–d) Tilt-view (tilt angle = 75°) SEM images of single-layered arch bridges with different height and span.

requirement of the arch parameters. Nanofiber probes are used for picking and placing the NW at the desired location and also for raising the central part. Second, one end of the NW is fixed on the Au electrode by the photothermal-induced nanobonding technique. Therefore, the fixed end of the NW does not move while raising the central part of the NW. Third, a nanofiber is inserted beneath the central part of the NW to raise the central part of the NW. The nanofiber being conical in shape, it has variable diameter. Therefore, the arch height is adjusted as per requirement just by changing the position of the nanofiber. Fourth, the other end of the NW is fixed on another Au electrode. The two ends of the Ag NW are bonded on different electrodes, so that the current–voltage characteristic curve can be recorded to unravel its potential to be used in manufacturing and repairing nanoelectronic devices. Following this technique, we have fabricated single arch bridges with different height (ranging from ≈300 nm to ≈20 μm) and span (ranging from ≈25 to ≈70 μm). Three representative single arch nanobridges with variable height (11 μm, 12.5 μm, and 300 nm) and span (50, 57, and 25 μm) are shown in Figure 2b–d. A list of various fabricated arch nanobridges with different height and span is provided in Table S1 (Supporting Information). To visualize the suspended part of an arch nanobridge, a video recorded while changing the focal plane of the optical microscope objective is provided in Video S1 (Supporting Information).

To demonstrate another application of the arch bridge, we put a GNP (a few tens of nm thick and a few tens of μm in diameter), which can act like a microreflector for visible light, on top of the arch bridge (**Figure 3**a). The diameter of the NW is about 284 nm, and the weight of the GNP (thickness

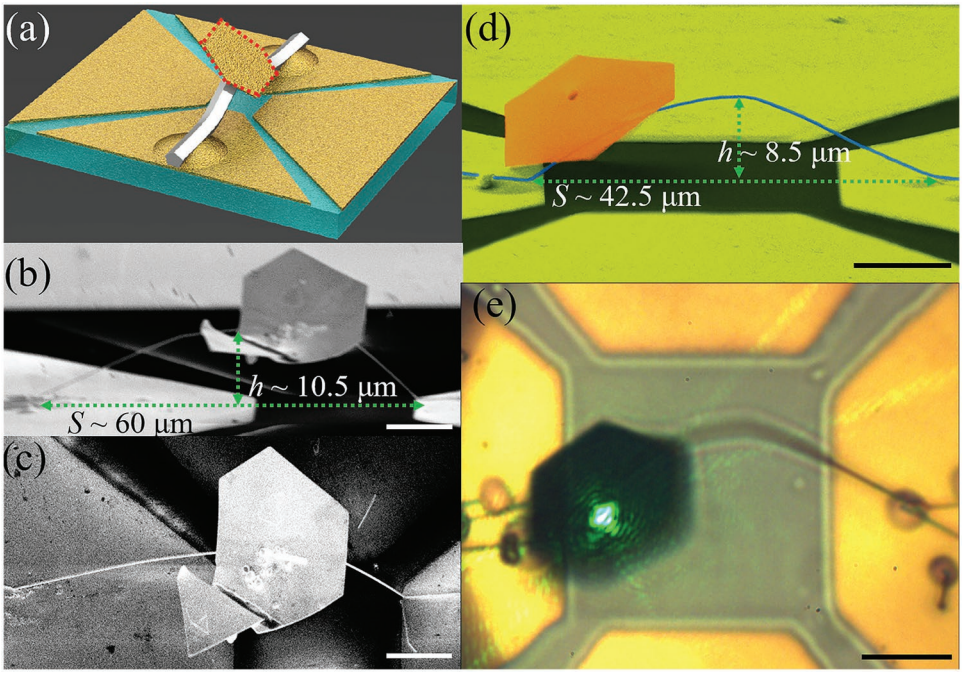

Figure 3. Gold nanoplate suspended on an arch nanobridge. a) Schematic diagram depicting a gold nanoplate (GNP) placed on top of a single arch bridge. b) Tilt- and c) top-view SEM images of a GNP suspended on an arch bridge. Tilt angle is set to be 75°. d) False colored tilt-view SEM image of another GNP placed on a nanobridge. e) Optical microscope image showing laser beam (532 nm) reflected from the GNP. The scale bars are 10 μm.

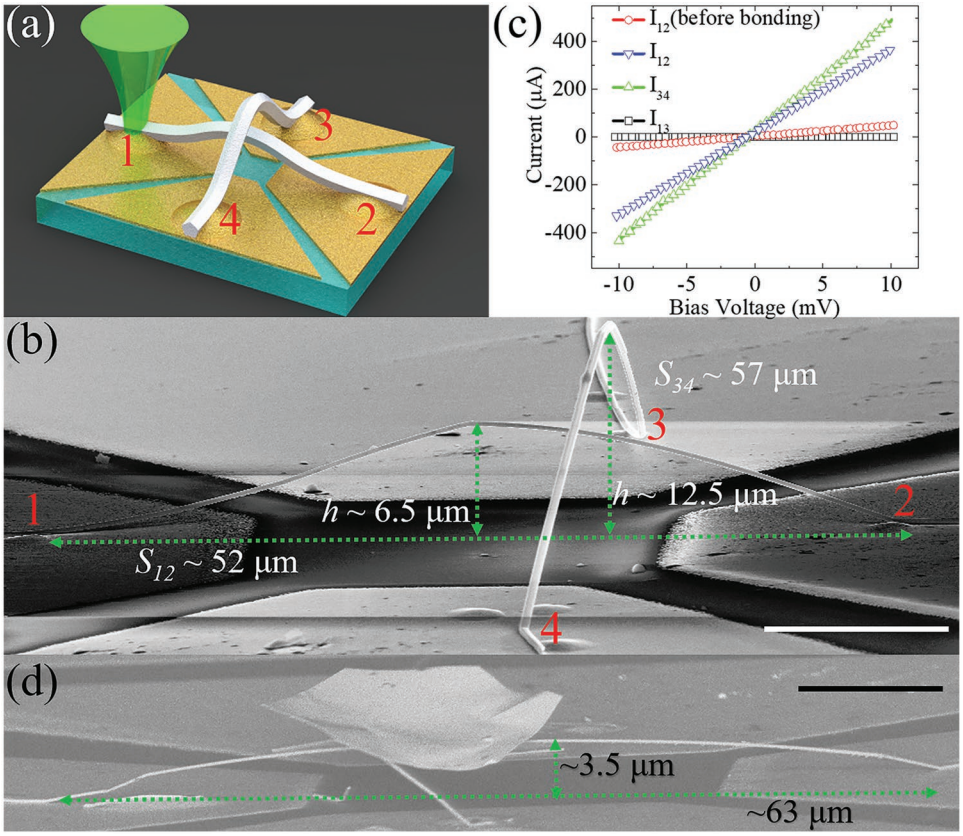

Figure 4. Multilayered arch nanobridge. a) Schematic diagram and b) tilt-view SEM image of a double-layered arch bridge. c) Current–voltage characteristic curves obtained for before and after the fabrication of the bridges. The rest of the current–voltage curves are obtained after bonding the NWs on the four different electrodes, and the subscripts indicate the electrode number as shown in (b). d) Tilt-view SEM image of a gold nanoplate placed on top of a double-layered nanobridge. Tilt angle is set to be 75°.

≈ 30 nm, average D ≈ 24 μm) is about 2.6 pN. Although the gold nanoplate is about 16 times heavier than the silver nanowire of the same length, the tilt and top view of the SEM image (Figure 3b,c) show no sign of bending or deformation of the bridge due to the weight on top of it, which indicates that the bridge is mechanically strong enough to keep such weight suspended in the air without buckling. One more example of a GNP suspended on top of a single arch nanobridge is shown in Figure 3d. To demonstrate its potential to be used as a microreflector, it is shown to reflect laser beam (532 nm) under an optical microscope (Figure 3e). A video showing a nanofiber sweeping under the GNP is also provided in Video S2 (Supporting Information). This video shows that the nanofiber does not touch the NW and the GNP, which supports the fact that the GNP is completely suspended in the air.

Multilayered arch bridges consisting of metal NWs are important in microelectronic circuits for connecting multiple ports without short-circuit. As a proof of the concept, we have fabricated a double-layered arch bridge which consists of two arch bridges of different heights and positioned orthogonally (**Figure 4**a). The top bridge is fabricated first, and next the bridge with lower height is fabricated (Figure 4b).

The current–voltage characteristic curves corresponding to the NWs before and after bonding on the Au thin film are shown in Figure 4c. It is observed that the conductivity increases multifold after bonding the NWs, which indicates that the bonding drastically improves the electrical connection. The obtained resistances corresponding to the top and bottom NWs are 27 and 20 Ω, respectively. This difference in conductivity of the two bridges is attributed to the larger diameter (525 nm) of the NW connecting the electrodes 3-and-4 compared to the diameter (370 nm) of the NW connecting 1-and-2. The zero conductivity between the electrodes 1-and-3 indicates no short-circuit, which is ensured by the height difference of about 6 μm between the top and bottom bridges. This feature demonstrates its potential applicability as short-circuit-free multipronged electronic connections in nanoelectronic devices. Furthermore, we have put a GNP on top of another double-layered arch bridge (Figure 4d) to demonstrate its mechanical strength.

Finally, toward demonstrating the mechanical robustness of the bonding, we also fabricated nanocantilever structures by binding one end of an Ag NW on an Au thin film and raising the other end using a nanofiber. Furthermore, we put a GNP (thickness ≈ 30 nm, average D ≈ 26 μm) on the suspended end of the nanocantilever (**Figure 5**a). The Ag NW (D ≈ 270 nm) makes an angle 44° with the horizontal plane, and the arm length is ≈30 μm, which keeps the GNP suspended horizontally in the air at a height ≈ 20 μm from top plane of the substrate (Figure 5b,c). The angle of the cantilever can be

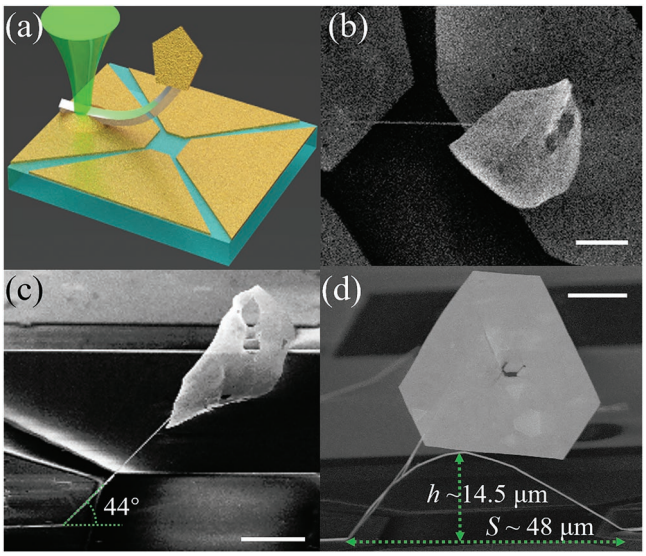

Figure 5. Nanocantilever. a) Schematic diagram of a nanocantilever. b) Top- and c) tilt-view SEM images of a gold nanoplate placed on top of the nanocantilever in a horizontal position. d) Tilt-view SEM image of a gold nanoplate placed on top of a nanocantilever in vertical position. A nanobridge is also fabricated under the nanocantilever, but the gold nanoplate is suspended in the air and not supported by the nanobridge. Tilt angle is set to be 75°. The scale bars are 10 μm.

manipulated by the nanofiber, which shows the flexibility of this fabrication technique. The adhesive force between the Ag NW and the GNP is strong enough to hold the GNP in a stable position, which indicates that the adhesive force is much greater than 3 pN (weight of the GNP). The gold nanoplate is about 20 times heavier than the silver nanowire of the same length indicating the super mechanical strength of the nanocantilever. Another example of a GNP suspended on nanocantilever vertically is shown in Figure 5d. This nanocantilever structure can potentially be used as a stand for a micro-object for a complex 3D optical or a mechanical system. A video showing a nanofiber sweeping under the GNP suspended in the air is also provided in Video S3 (Supporting Information). This video shows that the nanofiber neither touches the NW nor the GNP, which supports the fact that the GNP is completely suspended in the air.

In summary, we demonstrate the fabrication of multilayered arch bridges and cantilever structures consisting of Ag NWs by fixing the ends of the NWs on gold thin film by utilizing photothermal-induced nanobonding technique. The height (ranging from ≈300 nm to ≈20 μm) and span (ranging from ≈25 to ≈70 μm) of the fabricated bridges are varied over a wide range. The recorded current–voltage characteristic curves show superior electrical connection between the NW and the gold electrodes. Furthermore, we demonstrate the super mechanical strength of the nanobridges and nanocantilever by putting weight (about 20 times heavier than the Ag NWs of the same length) on top, and also use them as stand to hold micro-objects suspended in the air. For example, gold nanoplates, which can be used as microreflectors for visible light beam, are kept on top of the arch bridges and cantilever structures in a stable configuration. The multilayered arch nanobridges demonstrate their potential applicability as short-circuit-free multipronged electronic connections in nanoelectronic devices. Furthermore, by recording the change in vibration frequency due to proximity of contamination, these nanobridges and the nanocantilevers can be utilized as biological sensors. Fabrication of these arch nanobridges with superior electrical conductivity and super mechanical strength is a step forward toward realizing their true potential for nanoelectronic, nanophotonic, and nanomechanical devices.

Experimental Section

Simulation of Absorption and Electromagnetic Field Distribution: 3D FDTD method (FDTD Solutions v8.13, Lumerical) was used to obtain the fraction of the power from the source that is absorbed within the volume and the electromagnetic field distribution. From the FDTD results, the heat power volume density Q is calculated using the relation $Q = \frac{1}{2}\varepsilon_0 \omega \mathrm{Im}(\varepsilon_r)|E|^2$, where ε_0, ω, ε_r, and E are free space permittivity, angular frequency of the incident light, relative permittivity, and electric field, respectively.[50] For the simulation, a silver NW with a typical pentagonal cross section was considered to be placed on an Au thin film. Perfectly matched layers were set as absorbing boundary conditions. The maximum mesh sizes across the NW cross section and along the NW axis are fixed as 1.5 and 50 nm, respectively. The permittivity data for Au and Ag were taken from Johnson and Christy.[51] In the simulation, a Gaussian light source ($\lambda = 532$ nm) was considered to be focused on the junction of the NW and Au thin film.

Current–Voltage Curve: The current–voltage characteristic measurements were performed by a source-meter (Keithley 2602) and two tungsten microtapers. Two tungsten microtapers were touched on the electrodes connected with the NW, and the source-meter was used to scan the voltage and its corresponding current to obtain the *I–V* characteristic curves.

Supporting Information

Supporting Information is available from the Wiley Online Library or from the author.

Acknowledgements

The authors thank the supports from the National Key Research and Development Program of China (2017YFA0205700 and 2017YFE0100200) and National Natural Science Foundation of China (NSFC) (61425023, 61575177, and 61775194).

Conflict of Interest

The authors declare no conflict of interest.

Keywords

arch nanobridge, nanobonding, nanocantilever, nanofabrication, photothermal effect

Received: November 11, 2018
Revised: March 13, 2019
Published online: April 5, 2019

[1] R. H. Simpson, *Echos du monde classique: Classical views* **1998**, *XLII*, 239.
[2] J. Kim, W. A. Anderson, Y.-J. Song, G. B. Kim, *Appl. Phys. Lett.* **2005**, *86*, 253101.
[3] R. B. Lewis, P. Corfdir, H. Küpers, T. Flissikowski, O. Brandt, L. Geelhaar, *Nano Lett.* **2018**, *18*, 2343.
[4] R. F. Voss, R. B. Laibowitz, A. N. Broers, *Appl. Phys. Lett.* **1980**, *37*, 656.
[5] L.-C. Hsu, Y.-P. Kuo, Y.-Y. Li, *Appl. Phys. Lett.* **2009**, *94*, 133108.
[6] J. Y. Oh, M. S. Islam, *Appl. Phys. Lett.* **2014**, *104*, 022110.
[7] Y. Hong, D. Zhao, D. Liu, B. Ma, G. Yao, Q. Li, A. Han, M. Qiu, *Nano Lett.* **2018**.
[8] J. O. Lee, K.-W. Choi, S.-J. Choi, M.-H. Kang, M.-H. Seo, I.-D. Kim, K. Yu, J.-B. Yoon, *ACS Nano* **2017**, *11*, 7781.
[9] D. P. Langley, M. Lagrange, G. Giusti, C. Jimenez, Y. Brechet, N. D. Nguyen, D. Bellet, *Nanoscale* **2014**, *6*, 13535.
[10] Q. Li, Z. Chen, X. Zhang, Y. Peng, P. Ghosh, G. Yao, H. Luo, J. Lv, M. Qiu, *Opt. Lett.* **2018**, *43*, 4989.
[11] J. Ha, B. J. Lee, D. J. Hwang, D. Kim, *RSC Adv.* **2016**, *6*, 86232.
[12] L. Lin, G. Zou, L. Liu, W. W. Duley, Y. N. Zhou, *Appl. Phys. Lett.* **2016**, *108*, 203107.
[13] J. A. Spechler, C. B. Arnold, *Appl. Phys. A* **2012**, *108*, 25.
[14] E. C. Garnett, W. Cai, J. J. Cha, F. Mahmood, S. T. Connor, M. G. Christoforo, Y. Cui, M. D. McGehee, M. L. Brongersma, *Nat. Mater.* **2012**, *11*, 241.
[15] J. Mertens, A. Demetriadou, R. W. Bowman, F. Benz, M. E. Kleemann, C. Tserkezis, Y. Shi, H. Y. Yang, O. Hess, J. Aizpurua, J. J. Baumberg, *Nano Lett.* **2016**, *16*, 5605.
[16] J. H. Park, G.-T. Hwang, S. Kim, J. Seo, H.-J. Park, K. Yu, T.-S. Kim, K. J. Lee, *Adv. Mater.* **2017**, *29*, 1603473.
[17] S. Han, S. Hong, J. Ham, J. Yeo, J. Lee, B. Kang, P. Lee, J. Kwon, S. S. Lee, M.-Y. Yang, S. H. Ko, *Adv. Mater.* **2014**, *26*, 5808.
[18] G. Gonzalez-Rubio, J. Gonzalez-Izquierdo, L. Banares, G. Tardajos, A. Rivera, T. Altantzis, S. Bals, O. Pena-Rodriguez, A. Guerrero-Martinez, L. M. Liz-Marzan, *Nano Lett.* **2015**, *15*, 8282.
[19] J. Miao, S. Chen, H. Liu, X. Zhang, *Chem. Eng. J.* **2018**, *345*, 260.
[20] T. A. Celano, D. Hill, X. Zhang, C. W. Pinion, J. Christesen, C. J. Flynn, J. R. McBride, J. F. Cahoon, *Nano Lett.* **2016**, *16*, 5241.
[21] X. Liang, T. Zhao, P. Zhu, Y. Hu, R. Sun, C.-P. Wong, *ACS Appl. Mater. Interfaces* **2017**, *9*, 40857.
[22] S. S. Yoon, D. Y. Khang, *Nano Lett.* **2016**, *16*, 3550.
[23] R. Zhu, C.-H. Chung, K. C. Cha, W. Yang, Y. B. Zheng, H. Zhou, T.-B. Song, C.-C. Chen, P. S. Weiss, G. Li, Y. Yang, *ACS Nano* **2011**, *5*, 9877.
[24] H.-J. Lee, S. Oh, K.-Y. Cho, W.-L. Jeong, D.-S. Lee, S.-J. Park, *ACS Appl. Mater. Interfaces* **2018**, *10*, 14124.
[25] L. Dong, X. Tao, L. Zhang, X. Zhang, B. J. Nelson, *Nano Lett.* **2007**, *7*, 58.
[26] Z. Cheng, L. Liu, S. Xu, M. Lu, X. Wang, *Sci. Rep.* **2015**, *5*, 10718.
[27] P. Peng, A. Hu, A. P. Gerlich, G. Zou, L. Liu, Y. N. Zhou, *ACS Appl. Mater. Interfaces* **2015**, *7*, 12597.
[28] C. F. Guo, Y. Lan, T. Sun, Z. Ren, *Nano Energy* **2014**, *8*, 110.
[29] S. J. Lee, Y.-H. Kim, J. K. Kim, H. Baik, J. H. Park, J. Lee, J. Nam, J. H. Park, T.-W. Lee, G.-R. Yi, J. H. Cho, *Nanoscale* **2014**, *6*, 11828.
[30] S.-P. Chen, Y.-C. Liao, *Phys. Chem. Chem. Phys.* **2014**, *16*, 19856.
[31] J.-W. Do, D. Estrada, X. Xie, N. N. Chang, J. Mallek, G. S. Girolami, J. A. Rogers, E. Pop, J. W. Lyding, *Nano Lett.* **2013**, *13*, 5844.
[32] Y. Peng, T. Cullis, B. Inkson, *Nano Lett.* **2009**, *9*, 91.
[33] T.-B. Song, Y. Chen, C.-H. Chung, Y. Yang, B. Bob, H.-S. Duan, G. Li, K.-N. Tu, Y. Huang, Y. Yang, *ACS Nano* **2014**, *8*, 2804.
[34] Y. Yao, K. K. Fu, S. Zhu, J. Dai, Y. Wang, G. Pastel, Y. Chen, T. Li, C. Wang, T. Li, L. Hu, *Nano Lett.* **2016**, *16*, 7282.
[35] H. Yang, J. Lu, P. Ghosh, Z. Chen, W. Wang, H. Ye, Q. Yu, M. Qiu, Q. Li, *Appl. Phys. Lett.* **2018**, *112*, 071108.
[36] G. Pintu, L. Jinsheng, C. Ziyao, Y. Hangbo, Q. Min, L. Qiang, *Adv. Electron. Mater.* **2018**, *4*, 1700614.
[37] L. Zhou, J. Lu, H. Yang, S. Luo, W. Wang, J. Lv, M. Qiu, Q. Li, *Appl. Phys. Lett.* **2017**, *110*, 081101.
[38] J. van de Groep, P. Spinelli, A. Polman, *Nano Lett.* **2012**, *12*, 3138.
[39] F. Qian, P. C. Lan, M. C. Freyman, W. Chen, T. Kou, T. Y. Olson, C. Zhu, M. A. Worsley, E. B. Duoss, C. M. Spadaccini, T. Baumann, T. Y.-J. Han, *Nano Lett.* **2017**, *17*, 7171.
[40] B. Li, S. Ye, I. E. Stewart, S. Alvarez, B. J. Wiley, *Nano Lett.* **2015**, *15*, 6722.
[41] A. V. Akimov, A. Mukherjee, C. L. Yu, D. E. Chang, A. S. Zibrov, P. R. Hemmer, H. Park, M. D. Lukin, *Nature* **2007**, *450*, 402.
[42] K. M. Goodfellow, R. Beams, C. Chakraborty, L. Novotny, A. N. Vamivakas, *Optica* **2014**, *1*, 149.
[43] R. Ramachandramoorthy, W. Gao, R. Bernal, H. Espinosa, *Nano Lett.* **2016**, *16*, 255.
[44] Y. Chen, B. L. Dorgan Jr., D. N. McIlroy, D. E. Aston, *J. Appl. Phys.* **2006**, *100*, 104301.
[45] T.-G. Chen, B.-Y. Huang, H.-W. Liu, Y.-Y. Huang, H.-T. Pan, H.-F. Meng, P. Yu, *ACS Appl. Mater. Interfaces* **2012**, *4*, 6857.
[46] X. Li, H. Gao, C. J. Murphy, K. K. Caswell, *Nano Lett.* **2003**, *3*, 1495.
[47] P. Ghosh, J. Lu, H. Luo, Z. Xu, X. Yan, Y. Wang, J. Lu, M. Qiu, Q. Li, *Opt. Lett.* **2018**, *43*, 2422.
[48] H. Yang, M. Qiu, Q. Li, *Laser Photonics Rev.* **2016**, *10*, 278.
[49] N. Hartmann, D. Piatkowski, R. Ciesielski, S. Mackowski, A. Hartschuh, *ACS Nano* **2013**, *7*, 10257.
[50] X. Chen, Y. Chen, M. Yan, M. Qiu, *ACS Nano* **2012**, *6*, 2550.
[51] P. B. Johnson, R. W. Christy, *Phys. Rev. B* **1972**, *6*, 4370.

